Cyclodextrin-based supramolecular nanogels decorated with mannose for short peptide encapsulation

Archana Sumohan Pillai, Mohamed Achraf Ben Njima, Yasmine Ayadi, Laurent Cattiaux, Ali Ladram, Christophe Piesse, Benoit Baptiste, Jean-François Gallard, Jean-Maurice Mallet, Kawthar Bouchemal

Cyclodextrin-based Supramolecular Nanogels Decorated with Mannose for Short Peptide Encapsulation

Archana Sumohan Pillai,[a,b,#] Mohamed Achraf Ben Njima,[a,#] Yasmine Ayadi,[b] Laurent Cattiaux,[a] Ali Ladram,[c] Christophe Piesse,[d] Benoit Baptiste,[e] Jean-François Gallard,[f] Jean-Maurice Mallet,[a] Kawthar Bouchemal [*b]

Nanogels are aqueous dispersions of hydrogel particles formed by physically or chemically cross-linked polymer networks of nanoscale size. Herein, we devised a straightforward technique to fabricate a novel class of physically cross-linked nanogels via a self-assembly process in water involving α-cyclodextrin and a mannose molecule that was hydrophobically modified using an alkyl chain. The alkyl chain-modified mannose was synthesized in five steps, starting with D-mannose. Subsequently, nanogels were formed by subjecting α-cyclodextrin and the hydrophobically modified mannose to magnetic stirring in water. By adjusting the mole ratio between the hydrophobically modified mannose and α-cyclodextrin, nanogels with an average 100 - 150 nm diameter were obtained. Physicochemical and structural analyses by ^{1}H NMR and X-ray diffraction unveiled a supramolecular and hierarchical mechanism underlying the creation of these nanogels. The proposed mechanism of nanogel formation involves two distinct steps: initial interaction of hydrophobically modified mannose with α-cyclodextrin resulting in the formation of inclusion complexes, followed by supramolecular interactions among these complexes, ultimately leading to nanogel formation after 72 h of stirring. We demonstrated the nanogels' ability to encapsulate a short peptide ([*p*-^{t}BuF^{2}, R^{5}]SHf) as a water-soluble drug model. This discovery holds promise for potentially utilizing these nanogels in drug delivery applications.

1. Introduction

Monosaccharides typically bind to lectins through weak bonds, with dissociation constants usually falling from 10^{-3} M to 10^{-6} M [1, 2]. However, the development of glycoclusters incorporating sugars as multiple recognition domains for lectins has emerged as a potent method for enhancing binding affinity and specificity [3]. Various glycoclusters of diverse architectures, such as polymers, dendrimers, and nanoparticles, have been explored to generate multivalent interactions [4]. For a comprehensive review, refer to the work cited in reference [5]. Among the myriad multivalent systems, those based on cyclodextrin (CD) supramolecular assemblies hold particular interest. CDs, cyclic oligosaccharides derived from starch enzymatic degradation, exist in three native forms: α-CD, β-CD, and γ-CD, comprising 6, 7, or 8 units of glucose linked via α-1,4-glycoside bonds, respectively. CDs can form inclusion complexes with guest molecules, giving rise to a multitude of multivalent systems with variable degrees of complexity [6]. Under specific conditions, these inclusion complexes can form water-insoluble supramolecular assemblies like nanoparticles, microparticles, beads [7], or crystal structures with different morphologies [8].

In this context, a novel class of nanoparticles exhibiting a flattened morphology, termed nanoplatelets, was serendipitously developed by magnetically mixing α-CD with polysaccharides hydrophobically modified by alkyl chains [9-15]. Until now, those nanoplatelets are composed only of polysaccharides (*e.g.*, chitosan, heparin, dextran, amylopectin, pullulan, chondroitin sulfate, hyaluronic acid). The successful demonstration of particle design using monosaccharides has yet to be established. Herein, we exploited the property of α-CD to interact with alkyl chains to investigate the ability to design glycoclusters composed of mannose. Mannose was chosen as a ligand model to demonstrate the proof of concept. In this investigation, we first synthesized a mannose hydrophobically modified with a C17 alkyl chain and formulated it with α-CD via a self-assembly process in water. The resultant glycoclusters, designated nanogels, underwent comprehensive characterization from physicochemical and structural perspectives. Subsequently, we investigated the capability of these nanogels to encapsulate hydrophilic molecules. As a model of water-soluble active drug, we employed a potent analog of a natural antimicrobial peptide from the temporin family, temporin-SHf (SHf), isolated from the skin of the frog *Pelophylax saharicus* [16, 17]. SHf is the smallest natural linear antimicrobial peptide in vertebrates (8 amino acid residues) with the highest Phe residue content. The SHf analog [*p*-^{t}BuF^{2}, R^{5}]SHf [18] exhibited enhanced antimicrobial activity against Gram-positive and Gram-negative bacteria.

2. Experimental section

2.1. Materials. All solvents and chemical reagents were purchased from Sigma-Aldrich (Saint-Quentin Fallavier, France) and TCI (Zwijndrecht, Belgium) and used without further purification. Antimicrobial peptide [*p*-^{t}BuF^{2}, R^{5}]SHf, corresponding to the temporin-SHf analog F(*p*-^{t}BuF)FLRRIF-NH_2 (1200.43 g/mol), was

synthesized and characterized as published elsewhere [18]. Milli-Q® water was used for all the experiments (resistivity 18.2 MΩ.cm at 21 °C, Millipore purification system, Millex, SLAP 0225, Millipore, France).

2.2. Methods

2.2.1. Mannolipid synthesis and characterization

2.2.1.1. ML synthesis. Mannolipid (ML) was synthesized in 5 steps from D-mannose. The critical intermediate 3-azidopropyl 2,3,4,6-tetra-O-acetyl- α-D-mannopyranoside **1** (CAS 252210-04) was synthesized in two steps from D-mannose according to the literature from D-mannose peracetate and chloropropanol [19]. The azido group was reduced, and a stearoyl chain was added in a one-pot reaction using triphenylphosphine and stearoyl chloride [20] to give compound 2. This compound was next deprotected using sodium methylate in methanol (49% two steps).

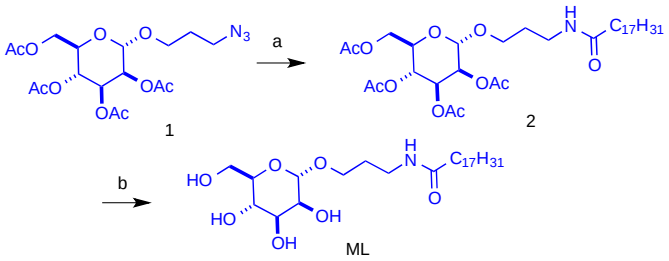

Scheme 1: a) $C_{17}H_{35}COCl$, Ph_3P, N,N-diisopropyl ethyl amine (DIEA), CH_2Cl_2, room temperature, 15 h, b) MeONa, methanol, room temperature, 5 h, 49% two steps.

For the synthesis of compound 2 in Scheme 1, triphenylphosphine (543 mg, 2.074 mmol, 1.3 equiv.) was added to a solution of azidopropyl 2,3,4,6-tetra-O-acetyl- α-D-mannopyranoside 1 (688 mg, 1.60 mmol, 1 equiv.) and stearoyl chloride (773 mg, 2.552 mmol, 1.6 equiv.) in dry CH_2Cl_2 (2 mL). The mixture was stirred overnight, and *N,N*-diisopropyl ethyl amine (DIEA, 330 µL, 1.914 mmol, 1.2 equiv.) was added. The reaction mixture was stirred for 15 min, diluted with CH_2Cl_2 (13 mL), and washed with 1 M HCl (2 × 5 mL), then a saturated solution of sodium bicarbonate (1 × 5 mL). The organic layer was dried over magnesium sulfate and concentrated. The residue was purified by flash chromatography (CyHex/AcOEt 60:40) to get compound **2** (1.0 g, 94%) (R_f: 0.23 (CyHex/AcOEt 60:40)). Details of ^{1}H NMR and ^{13}C NMR of compound 2 in Scheme 1 are given in the Supporting Information (SI) section.

ML was synthesized by adding sodium (30 mg) to a solution of compound 2 (1 g) in dry methanol (30 mL) at 0 °C. The solution was stirred from 0 °C to room temperature for 5 hours and then neutralized by Amberlyt IR 120 H^+ resin. The resin was filtered off, and the filtrate was concentrated *under a vacuum*. The crude product was purified by column chromatography on silica gel (CH_2Cl_2/ethanol 85:15) to get pure ML (390 mg, 49%, two steps) as a white powder. R_f: 0.26 (CH_2Cl_2/ethanol 85:15). The molecular weight of the obtained product was 504.3896 g.mol^{-1}, as characterized by mass spectrometry (Figure S1 in the SI).

2.2.1.2. ML chemical characterization. IR spectroscopic analysis of ML powder was conducted using an FT/IR-4100 JASCO spectrometer. Sixty scans were accumulated within the range of 4000 to 400 cm^{-1}. The resulting spectrum was analyzed using Spectra Manager software. Subsequently, the ML spectrum was compared to the D-mannose spectrum, and both were studied under identical conditions to discern any differentiating features. ^{1}H NMR, ^{13}C NMR, and ^{1}H, ^{13}C heteronuclear single quantum coherence (HSQC) spectroscopy was recorded on a Bruker instrument operating at a frequency of 300 MHz for ^{1}H NMR and HSQC and 75 MHz for ^{13}C NMR. Chemical shifts are given in parts per million (ppm) using solvent residual signals as the reference, and coupling constants (J) are given in Hertz (Hz).

2.2.2. Preparation of nanogel and nanogels encapsulating [p-^{t}BuF^2, R^5]SHf

2.2.2.1. Nanogel preparation. Nanogels were prepared by adding 5 mg of ML and α-CD (40, 70, 80, or 113 mg) in a small vial. The weight was then brought up to 1 g with the addition of water. A magnetic bar was added to each vial, and the preparations were stirred at 300 rpm for 72 h. The temperature was maintained constant at 25 °C. Notably, mixing speed and duration were selected as a starting point by adapting previous protocols optimized in our research group [21, 22]. Herein, the impact of mixing duration on preparation size was investigated at 12 h, 24 h, and 48 h of stirring of ML (5 mg/mL) and α-CD (70 mg/mL) in water.

ML suspension in water, used as a control, was prepared similarly without adding α-CD.

2.2.2.2. Preparation of nanogels encapsulating [*p*-^{t}BuF^2, R^5]SHf. Solution of [*p*-^{t}BuF^2, R^5]SHf was prepared in water at a concentration of 15 µg/mL in a small vial, 5 mg of ML and 70 mg of α-CD were added, then the weight was brought up to 1 g with [*p*-^{t}BuF^2, R^5]SHf solution. The suspension was magnetically stirred at 300 rpm for 72 h. The temperature was maintained constant at 25 °C. To evaluate the encapsulation efficiency (EE), the formulations were centrifuged at 3000 × g for 30 min, filtrated through a syringe filter (0.2 μm pore size), and the concentration of unloaded [*p*-^{t}BuF^2, R^5]SHf was determined by RP-HPLC analysis as published elsewhere [18].

Encapsulation efficiency representing the percentage of [*p*-^{t}BuF^2, R^5]SHf encapsulated in the nanogel calculated following Equation Eq.1.

$$EE = \frac{[[p\text{-}^t\text{BuF}^2,\ \text{R}^5]\text{SHf}]_{Nanogels}(\mu\text{g.})}{[[p\text{-}^t\text{BuF}^2,\ \text{R}^5]\text{SHf}]_{Suspension}(\mu\text{g.mL}^{-1})} \times 100 \qquad \text{Eq. 1}$$

Where $[[p\text{-}^t\text{BuF}^2,\ \text{R}^5]\text{SHf}]_{\text{Nanogels}}$ is the concentration of the antimicrobial peptide encapsulated in the nanogels and $[[p\text{-}^t\text{BuF}^2,\ \text{R}^5]\text{SHf}]_{\text{Suspension}}$ is the total concentration of the antimicrobial peptide in the suspension determined. The peptide concentration was analyzed using reverse-phase high-performance liquid chromatography (RP-HPLC) analysis (Table S1 in the SI).

2.2.3. Nanogel physicochemical characterization

2.2.3.1. Zeta potential. The particle surface potentials were calculated from the electrophoretic mobility using an electrophoretic light-scattering technique (Zetasizer Nanoseries, Malvern Instruments, Ltd., UK). For sample preparation, 40 µL of each suspension was diluted with NaCl (1 mM) (960 µL for the dilution 1/25 or 1960 µL for the dilution 1/50). Then, 1 mL of each

suspension was placed in a disposable folded capillary cell. Zeta potential was measured at 25 °C.

2.2.3.2. Dynamic light scattering. Nanogel mean hydrodynamic diameters (d_h) were measured by dynamic light scattering (DLS) using a Zetasizer Nanoseries. Each suspension (40 µL) was diluted in water (960 µL or 1960 µL for dilution 1/25 and 1/50, respectively) before analysis. Particle size was measured at 25 °C. The scattering angle was 173°. Each experiment was replicated three times on three independent formulations.

2.2.3.3. TEM. TEM characterizations were performed at 80 kV transmission using a transmission electron microscope (JEOL 1400) coupled to TEM Domain Centre software. Samples were prepared as detailed in our previous publication [22]. Typically, 1 µL suspensions were diluted in water (49 µL) and manually homogenized. Then, 4 µL suspensions were placed on a carbon grid. After 5 min of drying at room temperature, the grid was placed on a slide and inserted into the microscope for observation.

2.2.3.4. SEM. A Carl Zeiss MERLIN Field Emission-Scanning Electron Microscope (FE-SEM) operating at 5kV was used for morphological imaging. Samples were first diluted to 1/100 in water (99 µL water was added to 1 µL of nanogel suspensions and manually homogenized). Then, 25 µL of dilute liquid suspensions were directly dropped on freshly cleaved mica substrates held on sample holders with double sided carbon tape. To finish, preparations were dried at room temperature for 24 h and coated with 4 nm of a conductive layer of Palladium/Platinum alloy thanks to a Cressington 208 HR sputter-coater monitored with a thickness controller Cressington MTM 20.

2.2.4. Structural characterizations

2.2.4.1. NMR. ^{1}H NMR spectra were obtained by operating at 300 or 600 MHz (Bruker Avance, TXI SB 5 mm). The temperature was maintained at 298.15 K. The preparations composed of α-CD, ML, and α-CD/ML mixture were obtained as described for nanogels, except that water was replaced by DMSO-d6 or D_2O. NMR characterization of the interaction of the [*p*-^{t}BuF^2, R^5]SHf with α-CD was performed by ^{1}H NMR (600 MHz, DMSO-d6, 298.15 K) for the peptide ([*p*-^{t}BuF^2, R^5]SHf), α-CD/peptide, and α-CD/ML-peptide. The concentrations were 70 mg/mL for α-CD, 5 mg/mL for ML, and 15 µg/mL for the peptide. The preparations were mixed for 72 h before analysis. The ML and α-CD powders and glassware were dried under vacuum at 40 °C for 24 h before use.

2.2.4.2. XRD. Laboratory X-ray diffraction experiments were performed at the X-ray diffraction platform of the *Institut de Minéralogie, de Physique des Matériaux et Cosmochimie* (IMPMC), Sorbonne Université (Paris, France). A homemade diffractometer based on a Rigaku® MM007HF generator equipped with a Mo rotating anode (λKα1 = 0.709319 Å and λKα2 = 0.713609 Å) at 50 KeV and 24 mA was used. Combined with Osmic focusing multilayer optics, a RAXIS4++ image plate detector was placed at a distance of 300 mm from the samples; this set-up allowed the collection of high-quality 2D diffraction patterns from 2 to 42º 2θ in 15 min. The Fit2D program[23] was used to integrate 2D images into 1D patterns after calibration using a LaB6 standard crystalline sample.

3. Results and discussion

α-CD is a cyclic oligosaccharide comprising six glucose units linked by α-1,4-glycosidic bonds, yielding a truncated cone structure (Figure S2 in the SI section). Typically, α-CD exhibits dimensions ranging from 0.44 to 0.47 nm in width at the primary face and from 0.52 to 0.56 nm in width at the secondary face, with a height of approximately 0.7 to 0.8 nm. The cavity of α-CD could accommodate linear alkyl chains by forming inclusion complexes [24]. Under specific conditions, α-CD inclusion complexes could interact together, leading to supramolecular structures [25]. Building upon this understanding, this investigation aimed to exploit the interaction pattern between α-CD and linear alkyl chains to construct supramolecular structures incorporating a monosaccharide. D-mannose was chosen as the model sugar for proof of concept. First, an alkyl chain was covalently attached to D-mannose by adapting previously published protocols [19]. The alkyl chain length (C17) was determined based on our prior studies concerning α-CD-mediated supramolecular nanoassemblies [21, 22, 26-28].

3.1. ML characterization. ML chemical structure was characterized by IR and NMR. The IR spectrum of ML in Figure S3 exhibited characteristic peaks of mannose and aliphatic chains. The broad band between 3000 – 3500 cm^{-1} was attributed to the mannose's O–H stretching vibration (Figure S4, SI). The appearance of two bands at 2916 cm^{-1} and 2848 cm^{-1} after mannose hydrophobization corresponds to the symmetrical and asymmetrical elongation vibrations of –CH groups (Figure S3). A strong vibration band appeared at 1643 cm^{-1} for ML. This band is characteristic of an elongation vibration of the C=O group. A vibration band appeared at 1552 cm^{-1}, corresponding to the stretching and bending of amide II (C–N and C–N–H). We also noticed the appearance of a band at 1461 cm^{-1}, which corresponds to a secondary amine elongation vibration. The band at 1059 cm^{-1} is attributed to an elongation vibration of the –CH_2–O–C.

The ^{1}H NMR analysis of ML revealed distinctive signals representing different proton environments. At 0.86 ppm (Figure 1), a characteristic signal was identified for the –CH_3 end group. Intense and sharp peaks were observed at 1.24 ppm, corresponding to the fourteen –CH_2– groups constituting the heptadecamidopropoxy chain of ML (H2'-H15'). Refer to Figure S5 for the stereochemical configuration of ML with the proton numbering. Notably, the H16' peak at 1.47 ppm, closer to the electronegative C=O group, experienced a downfield shift, indicative of deshielding compared to the fourteen –CH_2– groups. The peak at 1.62 ppm correlated with the protons at the H19' position, demonstrating a downfield shift due to their proximity to electronegative groups, specifically oxygen and the amide. Further deshielding effects were observed in the methylene group directly attached to the C=O group (H17'). They were attributed to a peak at 2.03 ppm. Additionally, the peaks at 3.08 ppm were assigned to the signals of the –CH_2– group at position H18'.

The ^{13}C NMR spectrum in Figure S6 in the SI section exhibited distinctive carbon signals. The signal of the –CH_3 end group appeared at 13.3 ppm, while the –CH_2– groups ranged from 22.4 to 35.7 ppm. Carbon signals between 64.6 and 100.2 ppm were attributed to the carbons of mannose (specifically C1–C6, as

illustrated in Figure S6). Notably, the signal at 36.5 ppm was attributed to the carbon adjacent to the –NH– group (C9 in Figure S6), and the signal at 61.6 ppm corresponded to the carbon adjacent to the ether group –O– (C7 in Figure S6). Furthermore, the peak at 175.3 ppm corresponded to the amide bond (C=O) (as depicted in Figure S6). The α configuration of the mannopyrannoside ring was confirmed by the anomeric proton at 4.75 ppm (appearing as a singlet) and the anomeric carbon signal (100.2 ppm). The assignment of these signals was corroborated by proton/carbon correlation spectra (refer to Figure S7).

3.2. Nanogel physicochemical characterizations

3.2.1. Effect of mole ratios between α-CD and ML on nanogel physicochemical properties. At a concentration of 5 mg/mL, ML was insoluble in water without α-CD and without stirring, as depicted in Figure S8.a in the SI. A white suspension formed following a 72-hour magnetic stirring of ML in water (Figure S8.a' in the SI). TEM and SEM examinations revealed the presence of non-structured, indefinite-shaped objects (Figure S9). The SEM images at a 45° incline demonstrated the presence of thin objects stacked together (Figure S9.d).

Upon the addition of α-CD to the ML suspension and subsequent 72-hour magnetic stirring, homogenous whitish suspensions were obtained (Figure S8.b', c', d', e'). The respective mole ratios between α-CD and ML (referred to as $R_{\alpha\text{-}CD/ML}$) are provided in Table 1.

When ML was combined with α-CD at a ratio $R_{\alpha\text{-}CD/ML}$ of 4 (corresponding to ML and α-CD concentration of 5 mg/mL and 40 mg/mL, respectively), a suspension of particles was obtained (Figure 2.a,e). Their mean hydrodynamic diameter, as measured by DLS, indicated a Z-average of 606 ± 144 nm, while observations via TEM and SEM revealed smaller particles ranging in size from 50 to 100 nm (Figure 2.a,e, S10-S14 in the SI). It is worth noting that information obtained from TEM and SEM images may not always align perfectly with data acquired from DLS, given that the latter is an intensity-based technique [29]. In contrast, size analysis from TEM and SEM is number-based. Indeed, the Z-average represents the intensity-weighted mean hydrodynamic size of the ensemble of particles measured by DLS. For this reason, we also analyzed particle size distribution expressed in terms of particle number percentage. The results unveiled the presence of two distinct particle populations: a population of approximately 100 nm size accounted for roughly 90%, whereas the population of around 584 nm represented only 7% of the total particles (Table 1). When expressed by volume percentage, the larger nanogel population constituted approximately 95%, with the smaller particle population representing only 5%. Based on these findings, we propose that at an α-CD concentration of 40 mg/mL, suspensions comprise particles approximately 100 nm in size, as observed in TEM and SEM, while the significant population (around 600 nm) detected by DLS could correspond to aggregates of smaller particles. These findings are consistent with SEM observations, wherein certain nanogels were observed as individual entities, while others appeared agglomerated (Figures 2.e, S10-S16).

As the $R_{\alpha\text{-}CD/ML}$ increased from 4 to 7, the Z-average also increased to 1389 ± 81 nm for the 1/25 sample dilution (the same dilution as for $R_{\alpha\text{-}CD/ML}$ = 4). However, those results should be interpreted carefully, as we discovered that the nanogel Z-average is influenced by sample dilution (Table 1). Indeed, upon sample dilution to 1/50, the Z-average reduced to 302 ± 41 nm. This trend can be attributed to the higher concentration of nanogels at $R_{\alpha\text{-}CD/ML}$ 7 compared to $R_{\alpha\text{-}CD/ML}$ 4. Analysis of nanogel size distribution expressed in number at a 1/50 dilution revealed the presence of a nanogel population with a size of 158 nm. TEM and SEM observations of this sample confirmed that the size of individualized nanogels ranged between 130 and 140 nm (Figures 2.b). TEM observations indicated that at this α-CD concentration, nanogels exhibited enhanced contrast compared to a lower α-CD concentration (refer to Figures 2.b, S17-S20 in the SI). Some nanogels appeared aggregated (Figure S21-23 in the SI), while others were observed as distinct entities (Figure S24 in the SI). SEM observations highlighted the presence of particles within the range 200 – 400 nm for preparations obtained using α-CD concentration of 70 mg/mL (as depicted in Figure 2.f).

When the α-CD concentration increased to 80 mg/mL ($R_{\alpha\text{-}CD/ML}$ = 8) and 113 mg/mL ($R_{\alpha\text{-}CD/ML}$ = 11), SEM analysis revealed that preparations appeared more concentrated than for the two other preparations ($R_{\alpha\text{-}CD/ML}$ = 4 and $R_{\alpha\text{-}CD/ML}$ = 7) (visible in Figures 2.g and 2.h, respectively). DLS data for $R_{\alpha\text{-}CD/ML}$ = 8 revealed that the Z-average depends on the sample dilution (Table 1). At a dilution of 1/50, this sample comprised a population of nanogels whose size is 109 nm, expressed in number percentage. Analysis of size distribution expressed in intensity and volume percentages also revealed that a population of small-size particles (124 – 127 nm size) predominated (Table 1).

3.2.2. Kinetic study of nanogel formation. For the first proof of nanogel preparation following ML and α-CD mixing in water, we used previously published protocols on nanoplatelets involving the interaction of α-CD with the alkyl chain grafted onto polysaccharides [21, 22, 26-28]. To determine an appropriate mixing duration, we investigated the mean hydrodynamic diameters using DLS at various time intervals (12, 24, and 48 h). The ML and α-CD concentrations were maintained at 5 and 70 mg/mL, respectively ($R_{\alpha\text{-}CD/ML}$ = 7). Results outlined in Table S3 of the SI section indicated that the Z-average exceeded 2500 nm regardless of the mixing duration.

Analysis of size distribution in terms of intensity, volume, and number percentages unveiled variability within the same sample and mixing duration (Table S3 in the SI section). After 12 h of mixing, the initial measurement reported two populations (1789 nm (94%) and 5149 nm (6%) in number percentage). In contrast, subsequent measurements yielded disparate results: a single population at 2561 nm (100%) for the second measurement and two populations at 761 nm (57%) and 3792 nm (43%) for the third measurement (Table S3). Similar observations were made for samples mixed for 24 h. However, in samples mixed for 48 h, a population of smaller particles (410 – 652 nm in number percentage) emerged (Table S3).

The population of larger particles can be attributed to ML, which remains insoluble in water at the tested concentration. We hypothesize that these two molecules begin to interact upon adding α-CD to the ML suspension. A progressive increase in mixing

duration may enhance ML solubilization, as evidenced by the reduction in the percentage of the population of larger particles observed after 48 h of stirring. Previous studies have highlighted the stirring duration of α-CD with an alkyl chain as a crucial parameter for forming well-structured supramolecular nanoassemblies [21].

To provide a more comprehensive understanding of the mechanism underlying nanogel formation, NMR and XRD techniques were employed, as elaborated in the subsequent section.

3.3. Nanogel structural characterizations

3.3.1. NMR. Molecular interactions between ML and α-CD were initially elucidated using ^{1}H NMR in D_2O. However, due to ML's insolubility in water, its spectrum at a 5 mg/mL concentration exhibited no discernible peaks (Figure 3.a.i). Consequently, ^{1}H NMR analyses were conducted in DMSO-d6 (Figure 4.i) to circumvent this limitation. A comparative examination of the ^{1}H NMR spectra of ML, α-CD (Figure 4.ii), and the resulting α-CD/ML complex (Figure 4.iii) provided valuable insights into their host-guest interaction behavior. The complexation of ML with α-CD in DMSO-d6 induced changes in peak shapes, evidenced by the splitting of the alkyl chain peak compared to free ML, possibly due to the interaction of the alkyl chain with the α-CD cavity. Notably, the observable peaks in DMSO-d6 (Figure 4) were absent in D_2O (Figure 3), likely attributed to differences in solvent polarity. In D_2O, the addition of α-CD at a concentration of 40 mg/mL to ML suspension ($R_{\alpha\text{-}CD/ML}$ = 4) led to the appearance of peaks at 0.75, 1.12, 1.34, 2.10, and 3.16 ppm (Figure 3.a.ii and magnified view in Figure 3.b). The appearance of peaks following α-CD addition suggests the inclusion of ML within the hydrophobic cavity of α-CD, rendering free ML more soluble in D_2O.

A gradual decrease in the intensity of these ML peaks was observed (Figures 3.a, spectra (iii) to (v)) with an increase in concentration of α-CD from 70 to 113 mg/mL ($R_{\alpha\text{-}CD/ML}$ 7 and 11, respectively). At a lower concentration of α-CD (40 mg/mL, $R_{\alpha\text{-}CD/ML}$ 4), a limited number of α-CD molecules is available to fully interact with ML. The broader peaks of α-CD protons observed between 3.0–4.0 ppm for 40 mg/mL indicate that the complex might be less stable at this concentration. Whereas, with an increase in the concentration of α-CD from 70 to 113 mg/mL ($R_{\alpha\text{-}CD/ML}$ 7 and 11, respectively), α-CD proton peaks appear sharper along with a gradual decrease in the intensity of the ML peaks (Figures 3.a, spectra (iii) to (v)). This suggests a stable inclusion complex at higher α-CD concentrations. As the concentration of α-CD increases, more α-CD are available for binding to the ML until a point of saturation is attained. This interaction between alkyl chains and α-CD cavities due to the hydrophobic interactions or hydrogen bonding is expected and consistent with previous investigations on the encapsulation of such guests with α-CD [24].

3.3.2. XRD. The X-ray diffraction pattern of α-CD powder exhibits multiple diffraction peaks resulting from its crystalline and cage-like structure in its native state [30, 31]. Broad diffraction peaks were detected upon the inclusion of ML within the cavity of α-CD, as depicted in Figure 5, indicating the formation of inclusion complexes. These diffraction patterns bear a striking resemblance to the columnar packing characteristic of α-CD powder [32]. The observed 2ϑ and calculated d-spacing values are detailed in Figure 5 caption. The diffraction peak at 2ϑ = 11.6° corresponds to the cage structure of α-CD. The increased intensity of this peak with rising concentration suggests a proportional augmentation in the assembly of cage-like complexes as the concentration of α-CD increases. Based on these observations, the mechanism of nanogel formation likely involves two key steps: initial interaction between α-CD and ML, followed by the self-assembly of α-CD/ML inclusion complexes. This self-assembly process, driven by non-covalent interactions between α-CD molecules [33], ultimately forms physically crosslinked nanogel particles.

We postulated that the physically crosslinked nanogels might harbor aqueous domains capable of encapsulating hydrophilic substances. To explore this possibility, we employed a peptide ([*p*-^{t}BuF^2, R^5]SHf) as a model of a water-soluble active drug and examined its encapsulation within the nanogels in the subsequent section.

3.4. Evaluation of nanogel ability to encapsulate [*p*-^{t}BuF^2, R^5]SHf

The encapsulation was conducted using a formulation comprising α-CD/ML ($R_{\alpha\text{-}CD/ML}$ 7). To encapsulate [*p*-^{t}BuF^2, R^5]SHf within the nanogels, the peptide was introduced into the aqueous phase before adding the two ingredients, ML and α-CD. The encapsulation efficiency of [*p*-^{t}BuF^2, R^5]SHf in the nanogel suspension reached 36%, corresponding to a concentration of encapsulated [*p*-^{t}BuF^2, R^5]SHf of 21.7 µg/mL (18.1 µM) (Table 2). The encapsulation efficiency could be interesting if we consider the minimum inhibitory concentration (MIC = 6.25 µM) of [*p*-^{t}BuF^2, R^5]SHf against *E. coli* (ATCC 25922) [18]. Furthermore, the encapsulated [*p*-^{t}BuF^2, R^5]SHf concentration was lower than its IC_{50}, evaluated at 121 µM in macrophages [18].

The mechanism underlying peptide encapsulation is likely attributed to its entrapment within the aqueous domains of the nanogels as they are gradually formed during the interaction of ML and α-CD. Moreover, suspecting that α-CD may interact with the [*p*-^{t}BuF^2, R^5]SHf domains, we characterized its encapsulation within the nanogels using NMR. ^{1}H NMR spectrum of [*p*-^{t}BuF^2, R^5]SHf at a concentration of 15 µg/mL in DMSO-d6 was compared to the ^{1}H NMR of complexed α-CD/[*p*-^{t}BuF^2, R^5]SHf and α-CD/ML/[*p*-^{t}BuF^2, R^5]SHf (refer Figure S25 in SI). Figure S25 highlighted peptide peaks' disappearance and chemical shift in the NMR spectrum upon adding α-CD. The disappearance of peptide peaks at 1.23 ppm corresponding to the protons of Phe-*p*-^{t}Bu of *p*-^{t}BuF^2, R^5]SHf[18] and the chemical shift of the protons at 3.7 – 4.4 ppm as observed in the magnified spectra of Figure S25 could suggest peptide interaction with α-CD.

4. Conclusion and perspectives

In conclusion, our study demonstrates the successful design of self-assembled nanogels in an aqueous environment by combining a hydrophobically modified mannose with α-CD. The nanogel formation relies on the interaction between the α-CD cavity and ML. The resulting inclusion complexes of α-CD/ML subsequently

self-assemble into a supramolecular structure, observed after 72 h of magnetic stirring in water. This mixing duration was selected based on prior investigations on self-assembled particles composed of α-CD [21] and confirmed by ^{1}H NMR and XRD. Critical process parameters such as mixing duration higher than 72 h, mixing methods, and temperature can be fine-tuned to pave the way for future investigations. These adjustments will be subject to structural characterizations using 2D NMR and XRD for each experimental condition.

This research holds promise for various applications for tailoring nanogels with other monosaccharides, building upon our understanding of lectin-carbohydrate interactions [1, 34, 35]. Mannosylated nanogels, for instance, show potential for developing multivalent systems targeting specific sites. Furthermore, the foundational success observed with short antimicrobial peptides hints at potential drug encapsulation and controlled release applications, indicating a promising direction for further exploration.

5. Acknowledgments

The present work has benefited from the core facilities of Imagerie-Gif, (http://www.i2bc.paris-saclay.fr), a member of IBiSA (http://www.ibisa.net), supported by "France-BioImaging" (ANR-10-INBS-04-01), and the Labex "Saclay Plant Science" (ANR-11-IDEX-0003-02). We are thankful to Rémy Pires Brazuna for his technical assistance in the SEM observations and the electron microscopy facilities from the Institut de Chimie et des Matériaux Paris-Est (ICMPE), UMR 7182 CNRS-Université Paris Est Creteil, 94320, Thiais, France. The authors thank Olivier Lequin, Isabelle Correira, Frederic de Montigny, Hiba Khelifa, Jean-François Gallard, Benoit Baptiste, Malaury Simon, and Celine Fosse for scientific discussion and helpful advice.

6. Funding

Author KB received funding from the Institut Universitaire de France, the ANR-21-CE09-0015, and ANR-21-CE17-0032.

References

(1) Kiessling, L. L.; Pohl, N. L. Strength in numbers: non-natural polyvalent carbohydrate derivatives. *Chemistry & biology* **1996**, *3* (2), 71-77.
(2) Lee, Y. C.; Lee, R. T. Carbohydrate-protein interactions: basis of glycobiology. *Accounts of Chemical Research* **1995**, *28* (8), 321-327.
(3) Toone, E. J. Structure and energetics of protein-carbohydrate complexes. *Current Opinion in Structural Biology* **1994**, *4* (5), 719-728.
(4) Baker, A. N.; Hawker-Bond, G. W.; Georgiou, P. G.; Dedola, S.; Field, R. A.; Gibson, M. I. Glycosylated gold nanoparticles in point of care diagnostics: From aggregation to lateral flow. *Chemical Society Reviews* **2022**.
(5) Behren, S.; Westerlind, U. Novel Approaches To Design Glycan-Based Antibacterial Inhibitors. *European Journal of Organic Chemistry* **2023**, *26* (1), e202200795.
(6) He, Y.; Fu, P.; Shen, X.; Gao, H. Cyclodextrin-based aggregates and characterization by microscopy. *Micron* **2008**, *39* (5), 495-516.
(7) Memişoğlu, E.; Bochot, A.; Özalp, M.; Şen, M.; Duchêne, D.; Hincal, A. A. Direct formation of nanospheres from amphiphilic β-cyclodextrin inclusion complexes. *Pharmaceutical Research* **2003**, *20* (1), 117-125.
(8) Gref, R.; Amiel, C.; Molinard, K.; Daoud-Mahammed, S.; Sébille, B.; Gillet, B.; Beloeil, J.-C.; Ringard, C.; Rosilio, V.; Poupaert, J. New self-assembled nanogels based on host–guest interactions: characterization and drug loading. *Journal of Controlled Release* **2006**, *111* (3), 316-324.
(9) Lembo, D.; Donalisio, M.; Laine, C.; Cagno, V.; Civra, A.; Bianchini, E. P.; Zeghbib, N.; Bouchemal, K. Auto-associative heparin nanoassemblies: a biomimetic platform against the heparan sulfate-dependent viruses HSV-1, HSV-2, HPV-16 and RSV. *European Journal of Pharmaceutics and Biopharmaceutics* **2014**, *88* (1), 275-282.
(10) Galus, A.; Mallet, J.-M.; Lembo, D.; Cagno, V.; Djabourov, M.; Lortat-Jacob, H.; Bouchemal, K. Hexagonal-shaped chondroitin sulfate self-assemblies have exalted anti-HSV-2 activity. *Carbohydrate Polymers* **2016**, *136*, 113-120.
(11) Diaz-Salmeron, R.; Chaab, I.; Carn, F.; Djabourov, M.; Bouchemal, K. Pickering emulsions with α-cyclodextrin inclusions: Structure and thermal stability. *Journal of Colloid and Interface Science* **2016**, *482*, 48-57.
(12) Grisin, T.; Bories, C.; Loiseau, P. M.; Bouchemal, K. Cyclodextrin-mediated self-associating chitosan micro-platelets act as a drug booster against *Candida glabrata* mucosal infection in immunocompetent mice. *International Journal of Pharmaceutics* **2017**, *519* (1-2), 381-389. DOI: doi.org/10.1016/j.ijpharm.2017.01.048.
(13) Carn, F.; Nowak, S.; Chaab, I.; Diaz-Salmeron, R.; Djabourov, M.; Bouchemal, K. Autoassemblies of α-cyclodextrin and grafted polysaccharides: Crystal structure and specific properties of the platelets. *The Journal of Physical Chemistry B* **2018**, *122* (22), 6055-6063.
(14) Ahmed, Z.; Malli, S.; Diaz-Salmeron, R.; Destruel, P.-L.; Da Costa, A.; Guigner, J.-M.; Porcher, F.; Baptiste, B.; Ponchel, G.; Bouchemal, K. New insights on the structure of hexagonally faceted platelets from hydrophobically modified chitosan and α-cyclodextrin. *International Journal of Pharmaceutics* **2018**, *548* (1), 23-33. DOI: 10.1016/j.ijpharm.2018.06.035.
(15) Diaz-Salmeron, R.; Ponchel, G.; Gallard, J.-F.; Bouchemal, K. Hierarchical supramolecular platelets from hydrophobically-modified polysaccharides and α-cyclodextrin: Effect of hydrophobization and α-cyclodextrin concentration on platelet formation. *International Journal of Pharmaceutics* **2018**, *548* (1), 227-236.
(16) Abbassi, F.; Oury, B.; Blasco, T.; Sereno, D.; Bolbach, G.; Nicolas, P.; Hani, K.; Amiche, M.; Ladram, A. Isolation, characterization and molecular cloning of new temporins from the skin of the North African ranid Pelophylax saharica. *peptides* **2008**, *29* (9), 1526-1533.
(17) Abbassi, F.; Lequin, O.; Piesse, C.; Goasdoué, N.; Foulon, T.; Nicolas, P.; Ladram, A. Temporin-SHf, a new type of phe-rich and hydrophobic ultrashort antimicrobial peptide. *Journal of Biological Chemistry* **2010**, *285* (22), 16880-16892.
(18) André, S.; Washington, S. K.; Darby, E.; Vega, M. M.; Filip, A. D.; Ash, N. S.; Muzikar, K. A.; Piesse, C.; Foulon, T.; O'Leary, D. J. Structure–activity relationship-based optimization of small temporin-SHf analogs with potent antibacterial activity. *ACS Chemical Biology* **2015**, *10* (10), 2257-2266.
(19) Ma, J.; Wang, Q.; Yang, X.; Hao, W.; Huang, Z.; Zhang, J.; Wang, X.; Wang, P. G. Glycosylated platinum (iv) prodrugs demonstrated

significant therapeutic efficacy in cancer cells and minimized side-effects. *Dalton Transactions* **2016**, *45* (29), 11830-11838.
(20) Maunier, V.; Boullanger, P.; Lafont, D.; Chevalier, Y. Synthesis and surface-active properties of amphiphilic 6-aminocarbonyl derivatives of D-glucose. *Carbohydrate research* **1997**, *299* (1-2), 49-57.
(21) Diaz-Salmeron, R.; Ponchel, G.; Bouchemal, K. Hierarchically built hyaluronan nano-platelets have symmetrical hexagonal shape, flattened surfaces and controlled size. *European Journal of Pharmaceutical Sciences* **2019**, *133*, 251-263. DOI: 10.1016/j.ejps.2019.04.007.
(22) Diaz-Salmeron, R.; Cailleau, C.; Denis, S.; Ponchel, G.; Bouchemal, K. Hyaluronan nanoplatelets exert an intrinsic anti-inflammatory activity in a rat model of bladder painful syndrome/interstitial cystitis. *Journal of Controlled Release* **2023**, *356*, 434-447. DOI: https://doi.org/10.1016/j.jconrel.2023.03.014.
(23) Hammersley, A. FIT2D: a multi-purpose data reduction, analysis and visualization program. *Journal of Applied Crystallography* **2016**, *49* (2), 646-652.
(24) Scelle, J.; Vervoitte, H.; Bouteiller, L.; Chamoreau, L.-M.; Sollogoub, M.; Vives, G.; Hasenknopf, B. Size-dependent compression of threaded alkyldiphosphate in head to head cyclodextrin [3] pseudorotaxanes. *Chemical Science* **2022**, *13* (8), 2218-2225.
(25) Cosgun, S. N. K.; Tuncaboylu, D. C. Cyclodextrin-linked PVP/PEG supramolecular hydrogels. *Carbohydrate Polymers* **2021**, *269*, 118278.
(26) Diaz-Salmeron, R.; Da Costa, A.; Michel, J.-P.; Ponchel, G.; Bouchemal, K. Real-time visualization of morphology-dependent self-motion of hyaluronic acid nanomaterials in water. *International Journal of Pharmaceutics* **2021**, *609*, 121172.
(27) Diaz-Salmeron, R.; Michel, J.-P.; Hadji, H.; Gout, E.; Vivès, R. R.; Ponchel, G.; Bouchemal, K. Role of the interactions with CD44 and supported bilayer membranes in the cellular uptake of soft multivalent hyaluronan nanoparticles. *Colloids and Surfaces B: Biointerfaces* **2021**, 111916.
(28) Diaz-Salmeron, R.; Toussaint, B.; Cailleau, C.; Ponchel, G.; Bouchemal, K. Morphology-Dependent Bioadhesion and Bioelimination of Hyaluronan Particles Administered in the Bladder. *Advanced NanoBiomed Research* **2022**, *2* (5), 2100138.
(29) Farkas, N.; Kramar, J. A. Dynamic light scattering distributions by any means. *Journal of Nanoparticle Research* **2021**, *23* (5), 120.
(30) Hwang, M. J.; Bae, H. S.; Kim, S. J.; Jeong, B. Polyrotaxane hexagonal microfiber. *Macromolecules* **2004**, *37* (24), 8820-8822.
(31) Specogna, E.; Li, K. W.; Djabourov, M.; Carn, F.; Bouchemal, K. Dehydration, dissolution, and melting of cyclodextrin crystals. *The Journal of Physical Chemistry B* **2015**, *119* (4), 1433-1442.
(32) Rusa, C. C.; Bullions, T. A.; Fox, J.; Porbeni, F. E.; Wang, X.; Tonelli, A. E. Inclusion compound formation with a new columnar cyclodextrin host. *Langmuir* **2002**, *18* (25), 10016-10023.
(33) Harata, K.; Uekama, K.; Otagiri, M.; Hirayama, F.; Ogino, H. The Structure of the Cyclodextrin Complex. X. Crystal Structure of α-Cyclodextrin-Benzaldehyde (1: 1) Complex Hexahyderate. *Bulletin of the Chemical Society of Japan* **1981**, *54* (7), 1954-1959.
(34) Veerappan, A.; Subramaniyan, S. B. Lectin–Carbohydrate Interactions in Pathogenesis. In *Lectins: Innate immune defense and Therapeutics*, Springer, 2022; pp 165-183.
(35) Cecioni, S.; Imberty, A.; Vidal, S. Glycomimetics versus multivalent glycoconjugates for the design of high affinity lectin ligands. *Chemical reviews* **2015**, *115* (1), 525-561.

Figures

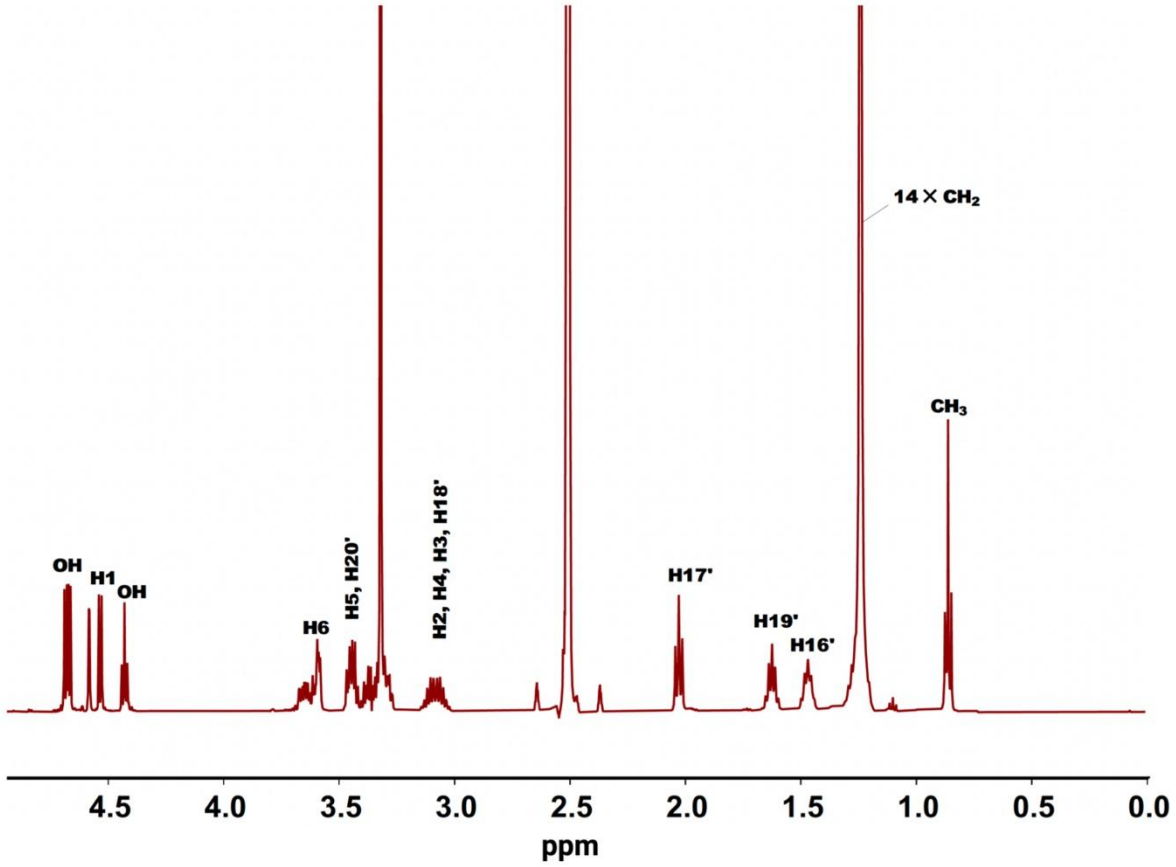

Figure 1: ^{1}H NMR spectrum (300 MHz, DMSO-d6, 298.15 K) of ML. The stereo-chemical configuration of ML is given in Figure S5 in the Supporting Information section.

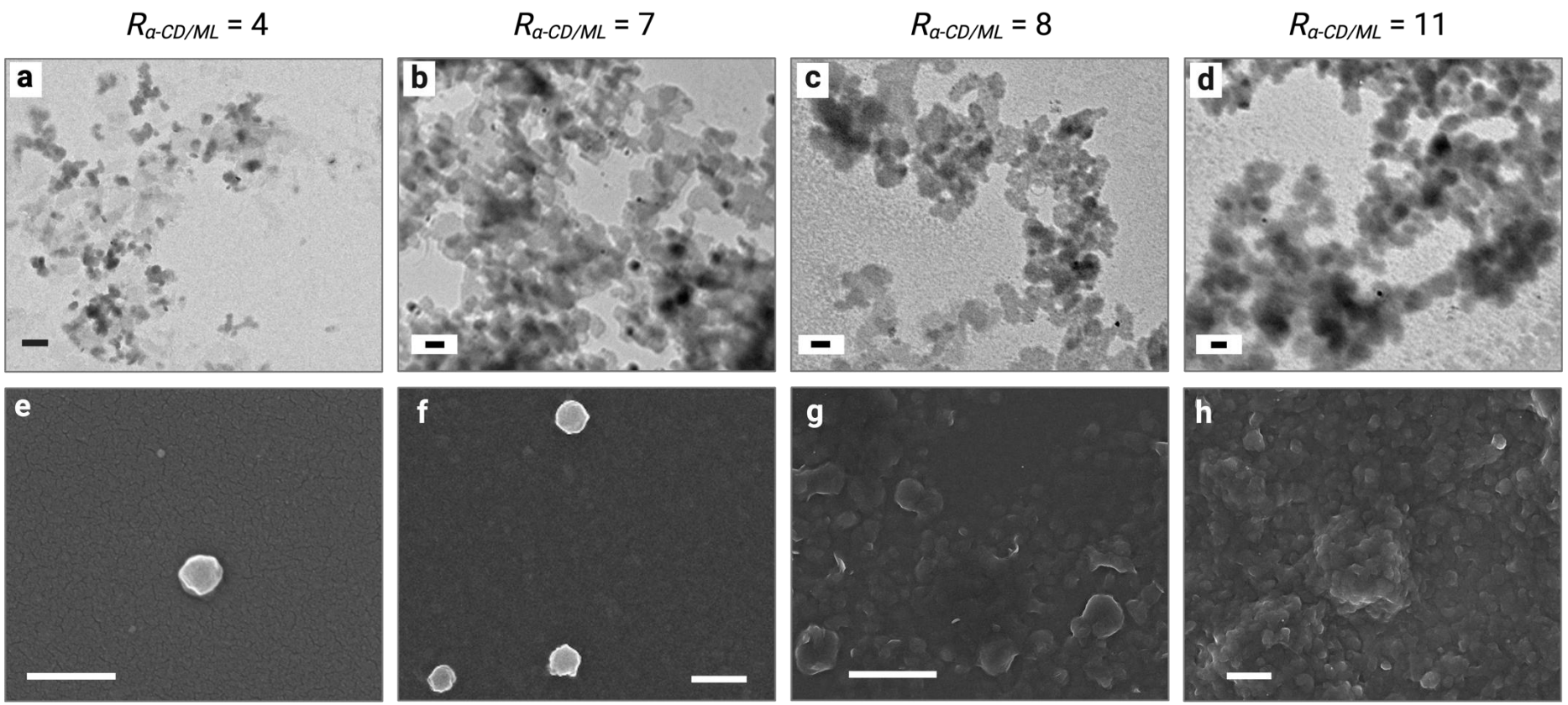

Figure 2: (a,b,c,d) TEM and (e,f,g,h) SEM images of α-CD/ML preparations were obtained after 72 h of magnetic stirring. ML concentration was maintained constant at 5 mg/mL and α-CD concentration was progressively increased as 40 mg/mL ($R_{\alpha\text{-}CD/ML}$ = 4) (a,e), 70 mg/mL ($R_{\alpha\text{-}CD/ML}$ = 7) (b,f), 80 mg/mL ($R_{\alpha\text{-}CD/ML}$ = 8) (c,g), and 113 mg/mL ($R_{\alpha\text{-}CD/ML}$ = 11) (d,h). Scale bars: a: 500 nm for (a,f), 200 nm for (b,d,c,d,e), 2 μm for (g), 1 μm for (h). Scale bars appear in black in (a,b,c,d) and white in (e,f,g,h).

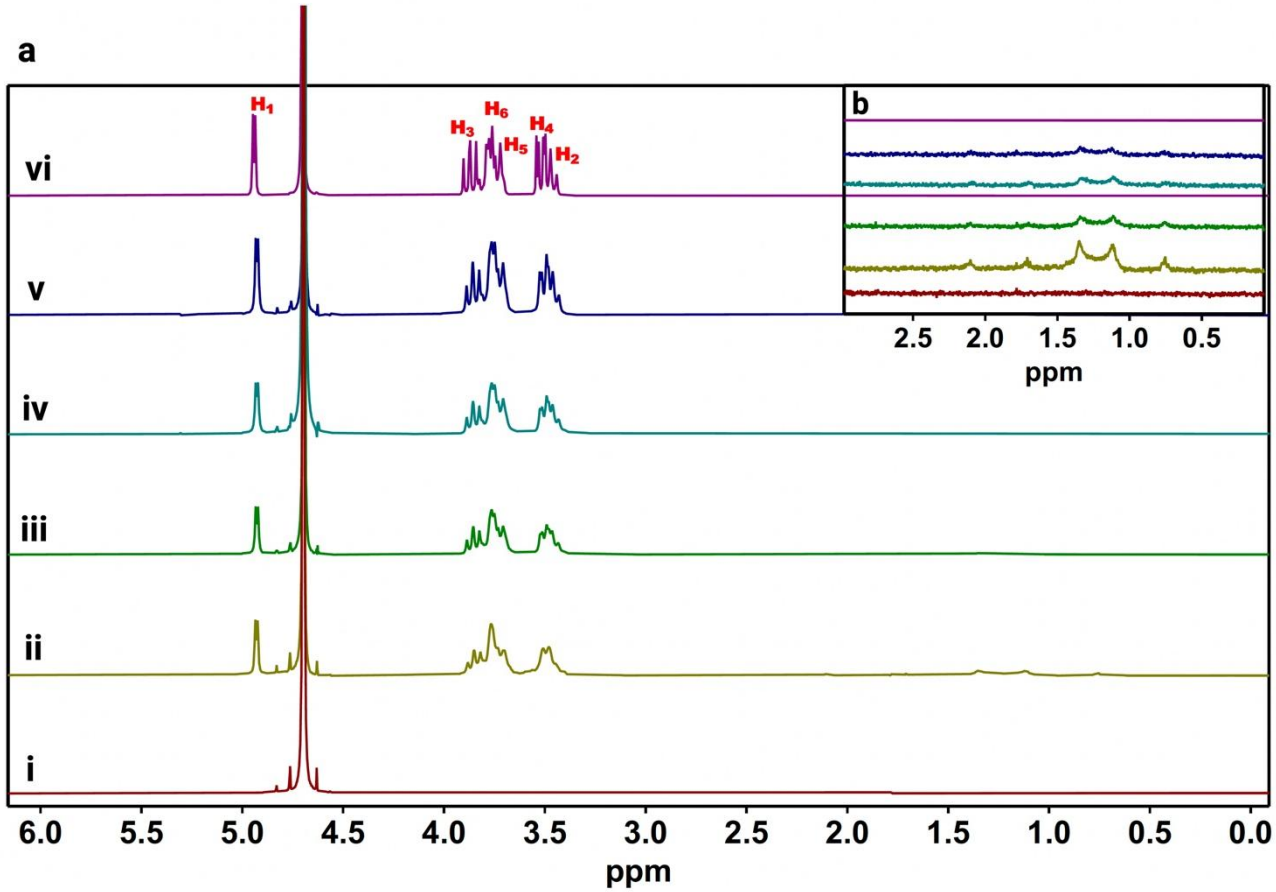

Figure 3: (a) ^{1}H NMR spectra (300 MHz, D_2O, 298.15 K) of [ML] = 5 mg/mL (i), and α-CD/ML after 72 h of stirring. [α-CD] was varied as 40 mg/mL ($R_{\alpha\text{-}CD/ML}$ = 4, spectrum (ii)), 70 mg/mL ($R_{\alpha\text{-}CD/ML}$ = 7, spectrum (iii)), 80 mg/mL ($R_{\alpha\text{-}CD/ML}$ = 8, spectrum (iv)), and 113 mg/mL ($R_{\alpha\text{-}CD/ML}$ = 11, spectrum (v)). The NMR spectrum of α-CD is given in (vi). A higher magnification of the spectra's 0 – 3 ppm region is presented in (b).

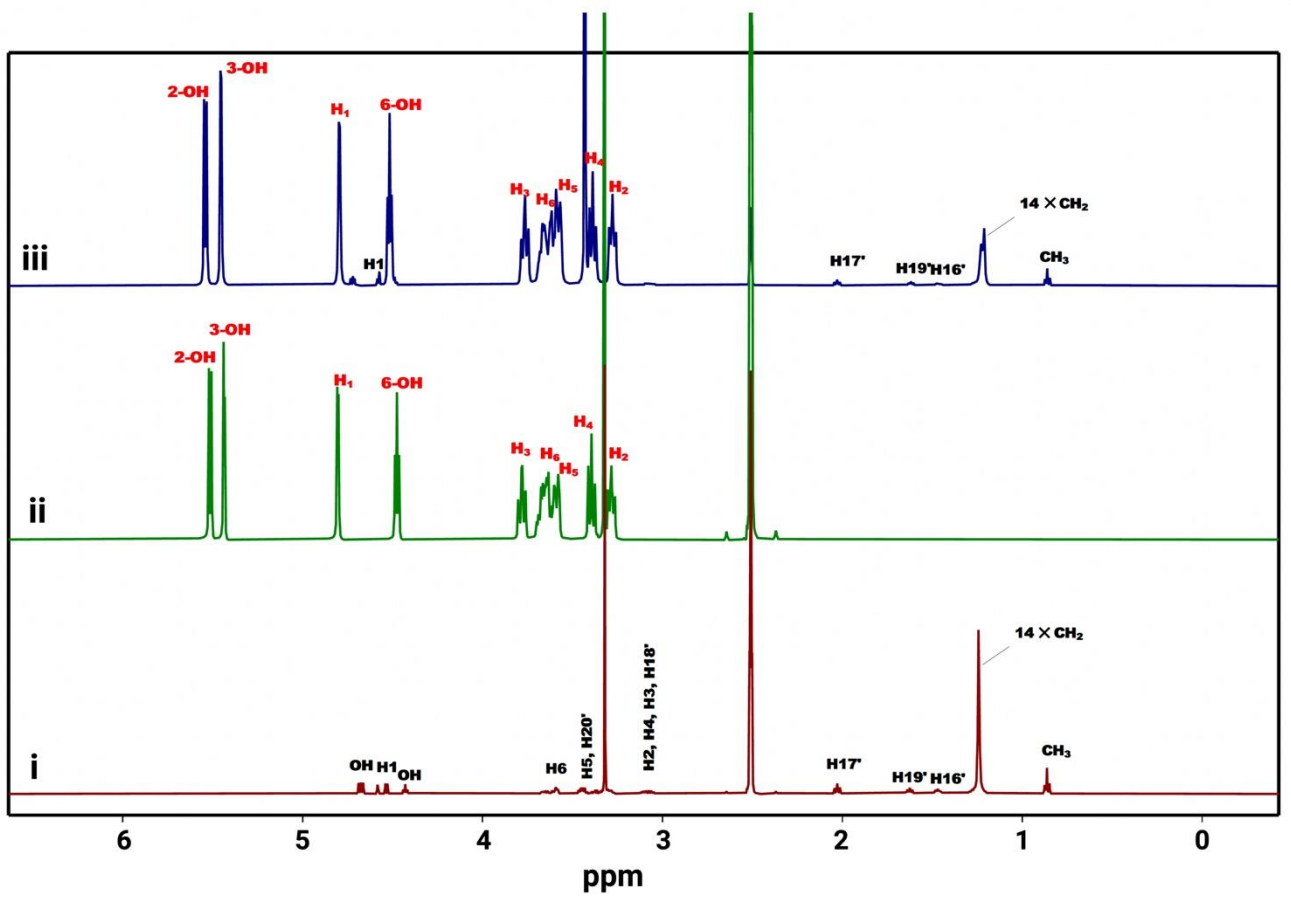

Figure 4: ^{1}H NMR spectra (600 MHz, DMSO-d6, 298.15 K) of ML (i), α-CD (ii), and α-CD/ML after 72 h of stirring (iii). Stereo-chemical configuration of the truncated conical structure of α-CD with interior and exterior protons and ML are indicated in Figures S2 and S5 in the SI section. [ML] = 5 mg/mL and [α-CD] = 70 mg/mL.

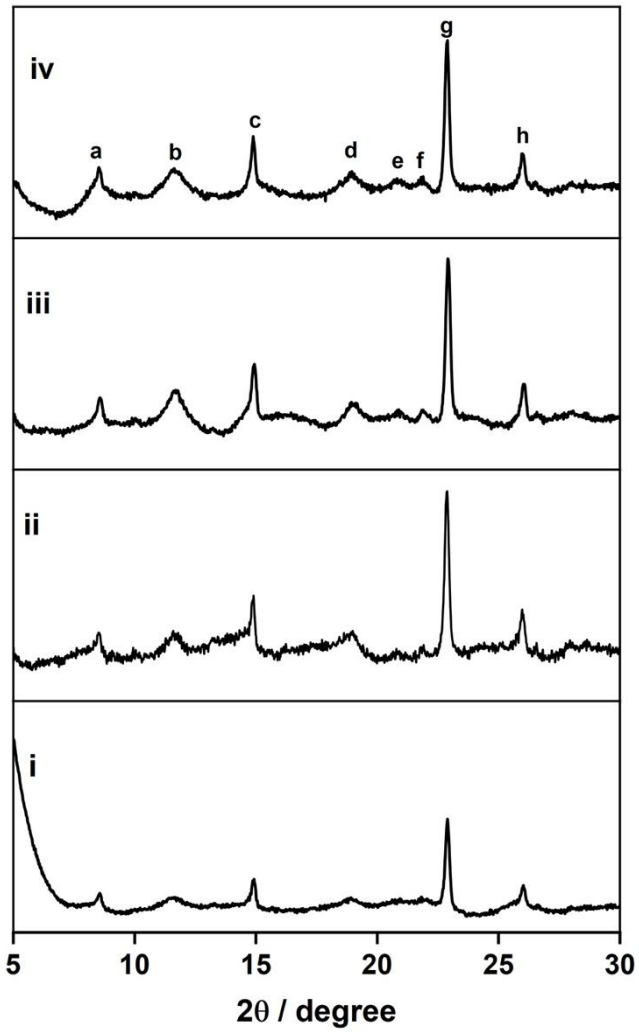

Figure 5: X-ray diffraction pattern of α-CD/ML nanogels. The concentration of ML was maintained at 5 mg/mL, while the concentration of [α-CD] was progressively increased: 40 mg/mL (i), 70 mg/mL (ii), 80 mg/mL (iii), and 113 mg/mL (iv). Nanogels were obtained after 72 h of stirring. (b) Values of 2ϑ and the crystallographic spacings for the α-CD/ML crystal structure are: (a): 2ϑ = 8.50, d-spacing: 10.39; (b): 2ϑ = 11.64, d-spacing: 7.59; (c): 2ϑ = 14.88, d-spacing: 5.94; (d): 2ϑ = 19.01, d-spacing: 4.61; (e): 2ϑ = 20.80, d-spacing: 4.26; (f): 2ϑ = 22. 90, d-spacing: 4.01; (g): 2ϑ = 22.89, d-spacing: 3.88; (h): 2ϑ = 25.98, d-spacing: 3.42.